Numerical modelling of methane-powered micro-tubular, single-chamber solid oxide fuel cell

N. Akhtar [a,b,*], S.P. Decent [a], K. Kendall [b]

[a] *School of Applied Mathematics, University of Birmingham, B15 2TT, UK*
[b] *Department of Chemical Engineering, University of Birmingham, B15 2TT, UK*

ABSTRACT

An experimentally validated, two-dimensional, axisymmetric, numerical model of micro-tubular, single-chamber solid oxide fuel cell (MT-SC-SOFC) has been developed. The model incorporates methane full combustion, steam reforming, dry reforming and water-gas shift reaction followed by electrochemical oxidation of produced hydrogen within the anode. On the cathode side, parasitic combustion of methane along with the electrochemical oxygen reduction is implemented. The results show that the poor performance of single-chamber SOFC as compared to the conventional (dual-chamber) SOFC (in case of micro-tubes) is due to the mass transport limitation on the anode side. The gas velocity inside the micro-tube is far too low when compared to the gas-chamber inlet velocity. The electronic current density is also non-uniform over the cell length, mainly due to the short length of the anode current collector located at the cell outlet. Furthermore, the higher temperature near the cell edges is due to the methane combustion (very close to the cell inlet) and current collection point (at the cell outlet). Both of these locations could be sensitive to the silver current collecting wire as silver may rupture due to cell overheating.

1. Introduction

Solid oxide fuel cells (SOFCs) are gaining increasing interest as a next-generation power sources with environmental friendly power generation. Though, most of the problems associated with performance and material issues have been resolved to a certain extent, commercial applications of SOFCs still suffer from limited durability and high costs [1,2]. One of the factors affecting the cell durability is the high-temperature operation requirement. The commonly used conventional electrolyte material (yttria-stabilized zirconia) requires an operational temperature of about 800° C in order to obtain an acceptable power output [3]. To reduce this operating temperature, the so-called intermediate-temperature solid oxide fuel cells (IT-SOFCs) are being developed, to allow longer life stainless steel interconnection [4–7].

The problems related to high cost mainly originate from the complex system design requirement for high-temperature SOFCs [8,9]. Since fuel flexibility is one of the major advantage of SOFCs, the most efficient strategy would be to use natural gas with high methane content for fueling the SOFCs [10]. Before, such gas is fed to the SOFC, it must be reformed either externally or internally. External reforming requires an additional reformer, thus

increasing the system's overall cost. On the other hand, internal reforming demands presence of steam, thereby diluting the fuel and reducing the overall performance. The other problem with internal reforming is its highly endothermic nature giving a lower inlet cell temperature and consequent poor output [11]. Another factor contributing to high systems cost is the bulky design, especially in case of planar cells, where high weight, large volume and complex sealing requirement could contribute significantly in terms of manufacturing cost [12–14].

Single-chamber solid oxide fuel cells (SC-SOFCs) have attracted recent attention because of their potential to reduce cost and provide simplicity in design [15]. The use of pre-mixed air/fuel mixture eliminates the necessity for external reforming, while avoiding the need for complex manifolding and sealing between the electrode compartments. Not only this, if micro-tubes are employed under mixed-reactant conditions, further benefits of quick start-up/shut down, high surface to volume ratio, and thermally shock resistant design can be realized [16,17].

The research work on SC-SOFC is mainly experimental as shown by a summary in Ref. [18]. While, most of the researchers focused on improving the power densities, a few of them reported the effective fuel utilization [18]. It should be noted that improving the power density by means of increasing the inlet fuel flow rate would result in lower fuel utilization, because only a certain part of the fuel will contribute to power production depending upon the operating conditions. Also, during experiments, the distribution of species, current density distribution and temperature distribution in a cell

* Corresponding author at: Department of Chemical Engineering, University of Birmingham, Edgbaston B15 2TT, UK. Tel.: +44 7726 126748; fax: +44 121 4143389.
E-mail address: nxa675@bham.ac.uk (N. Akhtar).

Nomenclature

$\mathbf{n}$	normal vector
$\mathbf{u}$	velocity vector
p	pressure
Y_i	mass fraction of the i th species
X_i	mole fraction of the i th species
h_i	specific enthalpy of the i th species
N	total number of species in the mixture
D_{ij}	binary diffusion coefficient for pair i–j
$\mathbf{j}_i$	mass diffusion flux of the i th species
r, z	axisymmetric coordinates
u	velocity in r direction
v	velocity in z direction
R	reaction rate
R_i	net reaction rate of the i th species
$\mathbf{F}$	momentum source term in the Brinkman equation
M	average (mixture) molecular weight
M_i	molecular weight of the i th species
R_g	universal gas constant
T	temperature
c_i	concentration of the i th species
B^{-1}	matrix function of inverted binary diffusion coefficients
B_{ii}	diagonal elements of inverted binary diffusion coefficient matrix
B_{ij}	non-diagonal elements of inverted binary diffusion coefficient matrix
D	matrix of Fick diffusion coefficients
$\mathcal{D}_{ij}$	Maxwell–Stefan diffusivity for pair i–j
V_i	molecular diffusion volume
CH_4	methane
CO_2	carbon dioxide
CO	carbon monoxide
H_2	hydrogen
O_2	oxygen
H_2O	water
N_2	nitrogen
e^{-1}	electron
O^{2-}	oxygen ion
D_{DG}^{eff}	Fick effective dusty gas diffusivity matrix
$D_{DG_{i,j}}^{eff}$	Fick effective dusty gas diffusivity for pair i–j
$\mathcal{D}_{DG_{i,j}}$	Maxwell–Stefan dusty gas diffusivity for pair i–j
$\mathcal{D}_{DG_{i,j}}^{eff}$	Maxwell–Stefan effective dusty gas diffusivity for pair i–j
$\mathcal{D}_{k,i}$	Knudsen diffusivity
$B_{DG_{ii}}^{eff}$	diagonal elements of inverted binary effective dusty diffusion coefficient matrix
$B_{DG_{ij}}^{eff}$	non-diagonal elements of inverted binary effective dusty diffusion coefficient matrix
d_p	average pore diameter
A	electrochemically active surface area of the medium per unit volume
Q	current source term
E	energy source term
ΔH	enthalpy of formation
i_a	anodic current density
i_c	cathodic current density
$i_{0,a}$	anodic exchange current density
$i_{0,c}$	cathodic exchange current density
V_c	cell voltage
V_{oc}	open circuit (Nernst) voltage

V^o	ideal (standard) voltage
z	number of electrons participating per electrochemical reaction
F	Faraday's constant
exp	exponent
k_s	thermal conductivity of solid (i.e. cell components)
$C_{p,s}$	specific heat of solid (i.e. cell components)
k_{eff}	effective thermal conductivity of solid and gas phase
ρ_{eff}	effective density of solid and gas phase
$C_{p,eff}$	effective specific heat of solid and gas phase
k	thermal conductivity of gas
C_p	specific heat of gas
ds	change in entropy generation
E_{act}	activation energy
R_{mix}	methane-to-oxygen ratio
D_t	micro-tube diameter
D_c	gas-chamber diameter
L_c	gas-chamber length

Greek symbols

∇	differential operator
∇^2	Laplace operator
ϕ_s	solid phase (electronic) potential
ϕ_e	electrolyte phase (ionic) potential
μ	dynamic viscosity
ρ	average (mixture) gas density
ρ_i	density of the i th species
ρ_s	density of solid (i.e. cell components)
Γ	thermodynamics matrix
κ	permeability
ϵ	porosity
ϵ_{rad}	radiative emmisivity
τ	tortuosity
π	constant (3.14159)
σ	conductivity
σ_o	Stefan–Boltzmann constant
α	charge transfer coefficient
γ	pre-exponential coefficient
η	overpotential

Subscripts

GC	gas-chamber
a	anode
e	electrolyte
c	cathode
rev	reversible
irr	irreversible
ohm	ohmic
act	activation
eff	effective
s	solid phase (electronic)
FOX	full combustion (oxidation)
SR	steam reforming
DR	dry reforming
SH	water-gas shift reaction
PAR	methane parasitic combustion

Superscripts

ref	reference
a	anodic
c	cathodic
d	methane parasitic index
f	oxygen parasitic index

is not so easy to determine. Furthermore, the gas velocity in the cell may differ from that supplied at the gas-chamber inlet. Calculation of gas velocities by modelling is therefore desirable.

Another benefit of modelling is the prediction of the species distribution inside the cells. During experimentation, it is not known whether the reactants are poorly depleted by the reaction products or fully consumed by complete combustion. If this is the case, then the remaining portion of the cell cannot generate enough power, therefore, the power density distribution could be non-uniform over the cell length. Furthermore, the operation of SC-SOFC with hydrocarbon/air mixtures is so complicated that the exact reaction mechanism on the anode side is still unknown. Most researchers have assumed partial oxidation of fuel in the anode, to generate hydrogen and carbon monoxide which then undergo electrochemical oxidation to produce electrical current [19–36]. But, it has been reported that the rate of carbon monoxide conversion via electrochemical oxidation is very slow [37]. Others have suggested that the partial oxidation of methane takes place via methane full combustion followed by steam and dry reforming over nickel anode [38–40]. Very recently, Hao and Goodwin [41] suggested three different reaction zones in the anode, i.e. a full combustion zone where hydrogen and carbon monoxide are oxidized at the gas–anode interface, followed by a methane wet-reforming zone, and a water-gas shift reaction zone deeper within the anode. If these reaction zones are existing within the anode thickness, then one would expect a temperature gradient deeper within the anode. Furthermore, the temperature at the anode–gas interface should be the dominant effect of a full combustion reaction mechanism. In our recent experimental study we have reported a temperature gradient of as high as 150° C over the cell length [42]. This steep temperature gradient is an indication of different reaction chemistry over the cell length which further supports the modelling results reported by Hao and Goodwin [41]. With the help of their modelling study and our previous experimental work, we were able to develop an improved numerical model discussed in detail below.

2. The mathematical model

In order to develop a mathematical model which can capture the experimental trends reported in our earlier study [42], we carried out a survey of the open literature. It was found that the proper implementation of the anode side reactions in an SC-SOFC should be the main focus of the model. We therefore emphasized the proper selection of anode side reactions with the help of available literature on partial oxidation of methane over nickel anodes. At this stage, we also included the temperature profiles along the cells as reported in our earlier experimental study [42]. The temperature trends are helpful in determining the extent of reforming/combustion activity over the cell length. With this information a set of possible reactions was postulated to narrow down the large window of reactions reported by Hao et al. (Table II in Ref.[41]). With a further study of literature, we found that the partial oxidation of methane over nickel anodes is itself a combination of three different reactions occurring within the anode [43–49]. The explanation for this behavior is reported as follows: The nickel catalyst quickly loses its reforming activity in the presence of oxygen. Over the oxidized catalyst only methane combustion proceeds. Therefore a substantial temperature increase is expected due to full combustion of methane near the cell inlet. Having consumed most of the oxygen at the inlet, the reforming reactions then take place over the rest of the cell length. Since reforming is an endothermic reaction, a decrease in temperature occurs downstream [43]. This observation was further supported by our experimental study, as we observed a nearly linear temperature drop over the cell length [42]. The high temperature measured at the inlet fully sup-

Table 1
Reactions in the anode [18,41,42].

Reaction	Equation	ΔH (kJ mol^{-1})
Methane full combustion	$CH_4 + 2O_2 \rightarrow 2H_2O + CO_2$	−803
Methane steam reforming	$CH_4 + H_2O \rightarrow 3H_2 + CO$	+206
Methane dry reforming	$CH_4 + CO_2 \rightarrow 2H_2 + 2CO$	+247
Shift reaction	$CO + H_2O \rightarrow H_2 + CO_2$	−33
Hydrogen electrochemical oxidation	$H_2 + O^{2-} \rightarrow H_2O + 2e^-$	n.k.

n.k. = not known.

Table 2
Reactions in the cathode [51].

Reaction	Equation	ΔH (kJ mol^{-1})
Methane full combustion	$CH_4 + 2O_2 \rightarrow 2H_2O + CO_2$	−803
Oxygen electrochemical reduction	$\frac{1}{2}O_2 + 2e^- \rightarrow O^{2-}$	n.k.

n.k. = not known.

ports the existence of full combustion of methane directly at the inlet, and the observed temperature drop downstream is expected to occur due to strong endothermic reforming reactions. Other reactions, like hydrogen and carbon monoxide combustion were excluded because their exothermic nature does not coincide with the existence of steep temperature gradients downstream. In conclusion, the short-listed reactions are: (1) methane full oxidation, (2) methane steam reforming, (3) methane dry reforming and (4) water-gas shift reaction followed by the electrochemical oxidation of produced hydrogen. The electrochemical oxidation of carbon monoxide is less preferred because of its slow reaction rate compared to hydrogen electrochemical oxidation [37]. Therefore, we assumed carbon monoxide will took part via the water-gas shift reaction, producing additional hydrogen. On the cathode side, parasitic combustion of methane is considered because the selectivity of cathode degrades with increase in temperature [50,51]. The possible reactions in the anode and cathode are summarized in Tables 1 and 2, respectively.

2.1. Model description

A micro-tubular geometry was opted as in the experimental setup. The cell consists of nickel, yttria-stabilized zirconia (Ni-YSZ) anode, yttria-stabilized zirconia (YSZ) electrolyte and yttria-stabilized zirconia, lanthanum strontium manganite (YSZ-LSM) cathode. In order to benefit from the symmetrical structure of the micro-tubular cell, a two-dimensional axisymmetrical setup has been considered. The dimensions of the gas chamber and cell are taken from our experimental study and are listed in Table 3. The diffusion parameters are given in Tables 4 and 5. All physical properties such as density, heat capacity, viscosity and thermal conductivity are considered as temperature dependent and their values are taken from Todd and Young [52]. Detailed formulation of mixture properties is presented in Ref. [52].

Table 3
Geometry dimensions [18,42].

Dimensions	Values (mm)
Gas-chamber length (L_c)	285
Gas-chamber diameter (D_c)	12
Micro-tube diameter (D_t)	1.6
Micro-tube length	55
Cathode active length	39
Anode thickness	200×10^{-3}
Cathode thickness	50×10^{-3}
Electrolyte thickness	15×10^{-3}

Table 4
Diffusion volumes in Fueller–Schettler–Giddings correlation parameters [61].

Molecule	Diffusion volume (cm^3 mol^{-1})
CH_4	24.42
CO_2	26.9
CO	18.9
H_2	7.07
O_2	16.6
H_2O	12.7
N_2	17.9

2.2. Model assumptions

- The flow is steady and fully developed.
- The carbon formation (coking) in the anode is neglected due to the presence of sufficient oxygen in the mixture [53].
- The ohmic heating (in the porous electrodes) due to electrical current transport is neglected because of high electrical conductivity as compared to the ionic conductivity [54].
- The electrolyte is a non-porous (dense, solid) material.
- The parasitic loss within the cathode (due to its non-ideal selectivity) is assumed to be due to methane combustion, which is temperature and pressure dependent [51].

In the following sections, each sub-domain is considered separately.

2.3. Computational domain

2.3.1. Gas-chamber

The gas chamber consists of a cylindrical glass tube with a micro-tubular cell placed in its center [Fig. 1]. The applicable equations are:

- Continuity equation:

$$\nabla \cdot (\rho \mathbf{u}) = 0 \tag{1}$$

- Momentum equation:

$$\rho(\mathbf{u} \cdot \nabla)\mathbf{u} = -\nabla p + \mu \nabla^2 \mathbf{u} + \frac{1}{3}\mu \nabla(\nabla \cdot \mathbf{u}) \tag{2}$$

Table 5
Maxwell–Stefan diffusion coefficients calculated using values given in Table 4.

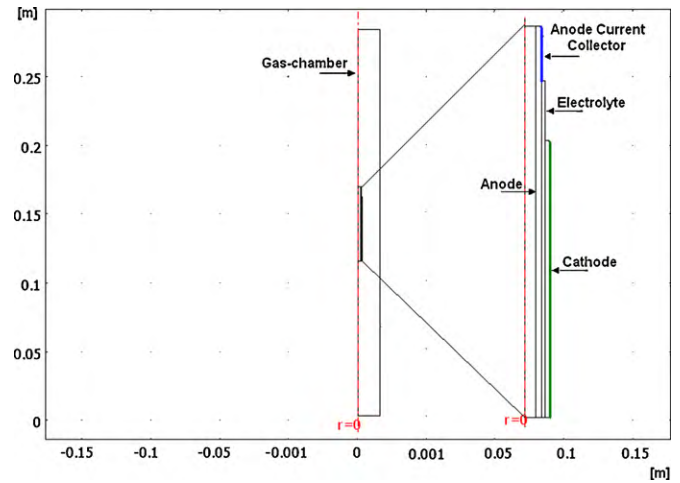| Molecular pair	$\mathcal{D}_{ij}$ (m^2 s^{-1})
CH_4–H_2O	2.3185×10^{-4}
CH_4–CO	1.8708×10^{-4}
CH_4–H_2	5.9505×10^{-4}
CH_4–CO_2	1.5516×10^{-4}
CH_4–O_2	1.9043×10^{-4}
CH_4–N_2	1.9034×10^{-4}
H_2O–CO	2.2382×10^{-4}
H_2O–H_2	7.5998×10^{-4}
H_2O–CO_2	1.8222×10^{-4}
H_2O–O_2	2.2849×10^{-4}
H_2O–N_2	2.2817×10^{-4}
CO–H_2	6.4243×10^{-4}
CO–CO_2	4.0176×10^{-4}
CO–O_2	4.0176×10^{-4}
CO–N_2	1.7738×10^{-4}
H_2–CO_2	5.5158×10^{-4}
H_2–O_2	6.7242×10^{-4}
H_2–N_2	6.5605×10^{-4}
CO_2–O_2	1.3970×10^{-4}
CO_2–N_2	1.4200×10^{-4}
O_2–N_2	1.7935×10^{-4}

Fig. 1. The geometrical setup.

- Species conservation equation:

$$\nabla \cdot (\rho \mathbf{u} Y_i + \mathbf{j}_i) = 0 \tag{3}$$

- Energy conservation equation:

$$\nabla \cdot \left(-k\nabla T + \rho C_p \mathbf{u} T + \sum_{i=1}^{N} h_i \mathbf{j}_i \right) = 0 \tag{4}$$

The density of the mixture is calculated using [55]:

$$\rho = \frac{1}{\displaystyle\sum_{i=1}^{N} Y_i / \rho_i} \tag{5}$$

The density of each species, ρ_i is obtained from the perfect gas law relation [55]:

$$\rho_i = \frac{p M_i}{R_g T} \tag{6}$$

Concentration of each species is calculated by:

$$c_i = \frac{p X_i}{R_g T} \tag{7}$$

where X_i is the mole fraction of the i th species which is related to the mass fraction Y_i by the following relation:

$$X_i = Y_i \left(\frac{M}{M_i} \right) \tag{8}$$

and

$$M = \sum_{i=1}^{N} X_i M_i \tag{9}$$

In Eq. (3) the multicomponent diffusive mass flux vector ($\mathbf{j}_i$) is described by the generalized Fick's law [56,57]:

$$\mathbf{j}_i = -\sum_{j=1}^{N-1} \rho D_{ij} \nabla Y_j \tag{10}$$

where N is the total number of species in the mixture.

D_{ij} in Eq. (10) is the multicomponent diffusion coefficient which in general is not symmetric ($D_{ij} \neq D_{ji}$). Also, the multicomponent D_{ij} does not have the physical significance of the binary Fick diffusivity

in that the D_{ij} do not reflect the i–j interactions [58]. Multicomponent diffusion coefficients D_{ij} are interrelated with Maxwell–Stefan diffusion coefficients $\mathcal{D}_{ij}$ through matrix B, such that [58]:

$$D = B^{-1}\Gamma \tag{11}$$

For ideal gases the thermodynamic matrix Γ reduces to the identity matrix and Eq. (11) becomes:

$$D = B^{-1} \tag{12}$$

where D is the multicomponent diffusion coefficient matrix and B is a square matrix of order $N - 1$ with elements given by:

$$B_{ii} = \frac{Y_i M}{M_i \mathcal{D}_{iN}} + \sum_{k=1, i \neq k}^{N} \frac{Y_k M}{M_k \mathcal{D}_{ik}} \tag{13}$$

$$B_{ij} = -\frac{Y_i M}{M_i}\left(\frac{1}{\mathcal{D}_{ij}} - \frac{1}{\mathcal{D}_{iN}}\right), \quad i \neq j \tag{14}$$

$\mathcal{D}$ in Eqs. (13) and (14) is the Maxwell–Stefan diffusion coefficients for binary pairs and is dependent on both temperature and pressure [59]. For gas pressures up to about 10 atmosphere at moderate to high temperatures, the diffusion coefficient for a binary mixture of gases i and j may be estimated from the Fueller, Schettler and Giddings relation [60]:

$$\mathcal{D}_{ij} = \frac{T^{1.75}(1/M_i + 1/M_j)^{1/2}}{p(V_i^{1/3} + V_j^{1/3})^2} \times 10^{-7} \tag{15}$$

where $\mathcal{D}_{ij}$ is the Maxwell–Stefan diffusion coefficient in $m^2 s^{-1}$, T is the temperature in kelvin (K), p is the pressure in atmospheres (atm), M_i is the molecular weight of molecules in $g\,mol^{-1}$, and V_i is the molecular diffusion volume in $cm^3\,mol^{-1}$. The values of V_i for different molecules are tabulated in [61]. Typical values of $\mathcal{D}_{ij}$ ($m^2 s^{-1}$) for molecules considered in this study are calculated using Eq. (15) and are given in Table 5 at a pressure of 1 atmosphere and at an average temperature of 1023 K, which is assumed to be the operating condition for the single-chamber solid oxide fuel cell in this study.

2.3.2. Gas diffusion electrodes

The gas diffusion electrodes consist of an anode and a cathode which are porous media. The following equations model gas diffusion electrodes:

• Continuity equation:

$$\nabla \cdot (\rho \mathbf{u}) = 0 \tag{16}$$

• Momentum equation: In porous media flow where viscous forces dominate convective ones, the momentum equation in the porous media may be modified from the Navier–Stokes equation to the Brinkman equation. In order to do so, the convective term has been neglected and an additional term for pressure drop in porous media, given by Darcy's law, has been added. This describes flow in porous media with a pressure gradient as the only driving force [62].

$$\nabla p = -\frac{\mu}{\kappa}\mathbf{u} \tag{17}$$

By inserting this term in the Navier–Stokes equation, we have the Brinkman equation as:

$$\frac{\mu}{\kappa}\mathbf{u} = -\nabla p + \mu \nabla^2 \mathbf{u} + \frac{1}{3}\mu \nabla(\nabla \cdot \mathbf{u}) + \mathbf{F} \tag{18}$$

where $\mathbf{F}$ is the source term that accounts for external force applied to the fluid due to production/consumption of species during fuel

cell reaction. This term is defined as [63]:

$$\mathbf{F} = \begin{bmatrix} R_i \mathbf{u} \\ R_i \mathbf{v} \end{bmatrix}$$

where R_i is the net reaction rate, which will be defined shortly.

• Species conservation equation:

$$\nabla \cdot (\rho \mathbf{u} Y_i + \mathbf{j}_i) = R_i \tag{19}$$

where $\mathbf{j}_i$ is the multicomponent diffusive mass flux vector in porous media, given by:

$$\mathbf{j}_i = -\sum_{j=1}^{N-1} \rho D_{DG}^{eff} \nabla Y_j \tag{20}$$

where D_{DG}^{eff} is the effective dusty gas diffusivity.

Diffusion in porous media is usually described by a molecular (particle–particle collision) and/or a Knudsen (particle–wall collision) diffusion mechanism [64]. In order to account for a detailed diffusion mechanism, both modes have been considered by implementing the dusty gas model (DGM). The DGM is derived by considering the solid matrix as large stationary spheres suspended in the gas mixture as one of the species present. The DGM diffusivity is then given by [64]:

$$\mathcal{D}_{DG_{i,j}} = \frac{\mathcal{D}_{ij}\mathcal{D}_{k,i}}{\mathcal{D}_{ij} + \mathcal{D}_{k,i}} \tag{21}$$

where

$$\mathcal{D}_{k,i} = \frac{1}{3}d_p\sqrt{\frac{8R_g T}{\pi M_i}} \tag{22}$$

The values of $\mathcal{D}_{ij}$ are calculated using Eq. (15) and the DGM diffusivities are further corrected using the following expression [64]:

$$\mathcal{D}_{DG_{i,j}}^{eff} = \left(\frac{\epsilon}{\tau}\right)\mathcal{D}_{DG_{i,j}} \tag{23}$$

Finally, the value of $\mathcal{D}_{DG_{i,j}}^{eff}$ is used to calculate the matrix $D_{DG_{i,j}}^{eff}$, having elements:

$$B_{DG_{ii}}^{eff} = \frac{Y_i M}{M_i \mathcal{D}_{DG_{i,N}}^{eff}} + \sum_{k=1, i \neq k}^{N} \frac{Y_k M}{M_k \mathcal{D}_{DG_{i,k}}^{eff}} \tag{24}$$

$$B_{DG_{ij}}^{eff} = -\frac{Y_i M}{M_i}\left(\frac{1}{\mathcal{D}_{DG_{i,j}}^{eff}} - \frac{1}{\mathcal{D}_{DG_{i,N}}^{eff}}\right), \quad i \neq j \tag{25}$$

The right hand side term, R_i, in Eq. (19) is the net reaction rate as a result of production/consumption of species. Since several reactions are taking place in the electrodes, simultaneously, the R_i term is calculated on the basis of net reaction rate on each electrode for each species. The corresponding reaction rates for each reaction and a net reaction rate for each species are given in Tables 6 and 7[65–68].

• Charge conservation equation:

The electronic charge transfer in the electrodes is described by a governing equation for the conservation of charge [54,64]:

$$\nabla \cdot (-\sigma_s^{eff} \nabla \phi_s) = Q_s \tag{26}$$

where Q_s is the electronic current source term. In the anode, this term is defined as:

$$Q_s = -A_a i_a \tag{27}$$

Table 6
Reaction rates and equilibrium constants [65–68].

Reaction rate (mol m^{-3} s^{-1})	Reaction rate constant
$R_{FOX} = k_1[CH_4][O_2]^{2.0}$	$k_1 = 3.0 \times 10^8 exp(-\frac{90,000}{RT})$
$R_{SR} = k_2[CH_4][H_2O] - k_3[CO][H_2]^{3.0}$	$k_2 = 2.3 \times 10^{-8}$, $k_3 = 1.4 \times 10^{-20}$
	$K_1 k_4 = 2.61 \times 10^{-3} exp(-\frac{4300}{T})$
$R_{DR} = \frac{K_1 k_4 * K_3 * k_5 *[CH_4][CO]}{K_1 k_4 * K_3 *[CH_4][CO_2] + K_1 k_4 *[CH_4] + K_3 k_5 *[CO_2]}$	$K_3 = 5.17 \times 10^{-5} exp(\frac{8700}{T})$
	$k_5 = 5.35 \times 10^{-1} exp(-\frac{7500}{T})$
$R_{SH} = k_6[CO][H_2O] - k_7[CO_2][H_2]$	$k_6 = 1.5 \times 10^{-7}$, $k_7 = 1.4 \times 10^{-7}$
$R_{PAR} = k_8[CH_4]^d[O_2]^f$	$k_8 = 3.0 \times 10^5 exp(-\frac{90,000}{RT})$
$R_{H_2} = -A_a i_a (M_{H_2}/2F)$	–
$R_{H_2O} = +A_a i_a (M_{H_2O}/2F)$	–
$R_{O_2} = -A_c i_c (M_{O_2}/4F)$	–

and in the cathode, this term is described as:

$$Q_s = +A_c i_c \tag{28}$$

The ionic charge transfer in the electrodes is given by [54,64]:

$$\nabla \cdot (-\sigma_e^{eff} \nabla \phi_e) = Q_e \tag{29}$$

where Q_e is the ionic current source term. In the anode, this term is defined as:

$$Q_e = -A_a i_a \tag{30}$$

and in the cathode, this term is described as:

$$Q_e = +A_c i_c \tag{31}$$

The anode and cathode side current densities (i_a and i_c, respectively) are calculated from the Butler–Volmer equation [69]:

$$i_a = i_{0,a} \left[exp\left(\frac{\alpha_a^a F \eta_{act_a}}{R_g T}\right) - exp\left(-\frac{\alpha_c^a F \eta_{act_a}}{R_g T}\right) \right] \tag{32}$$

$$i_c = i_{0,c} \left[exp\left(\frac{\alpha_a^c F \eta_{act_c}}{R_g T}\right) - exp\left(-\frac{\alpha_c^c F \eta_{act_c}}{R_g T}\right) \right] \tag{33}$$

The exchange current densities, $i_{0,a}$ and $i_{0,c}$ are expressed as a function of local partial pressure of the species [54]:

$$i_{0,a} = \gamma_a \left(\frac{p_{H_2}}{p^{ref}}\right) \left(\frac{p_{H_2O}}{p^{ref}}\right)^{-0.5} exp\left(\frac{-E_{act,a}}{R_g T}\right) \tag{34}$$

$$i_{0,c} = \gamma_c \left(\frac{p_{O_2}}{p^{ref}}\right)^{0.25} exp\left(\frac{-E_{act,c}}{R_g T}\right) \tag{35}$$

where p^{ref} is the reference pressure in the gas-chamber, i.e. the total pressure of 1 atm. γ_a and γ_c are the anodic and cathodic pre-exponential coefficients, $E_{act,a}$ and $E_{act,c}$ are the anodic and cathodic activation energies, respectively.

The anode and cathode side activation overpotentials are calculated by [70]: $\eta_{act_a} = \phi_{s,a} - \phi_{e,a}$ = anode side activation overpotential. $\eta_{act_c} = \phi_{s,c} - \phi_{e,c} - V_{oc}$ = cathode side activation overpotential.

where $\phi_{s,a}$ and $\phi_{e,a}$ are respectively the solid phase (electronic) and electrolyte phase (ionic) potential in the anode, $\phi_{s,c}$ and $\phi_{e,c}$ are the electronic and ionic potential in the cathode, and V_{oc} is the open circuit (Nernst) voltage, as expressed by [71]:

$$V_{oc} = V^o + \frac{R_g T}{2F} ln\left(\frac{p_{H_2}}{p_{H_2O}}\right) + \frac{R_g T}{4F} ln(p_{O_2}) \tag{36}$$

• Energy conservation equation:

Energy transport in the gas diffusion electrodes is modelled by considering the porous nature of the electrodes. Instead of using the thermal conductivity (k_s), density (ρ_s) and specific heat ($C_{p,s}$) of the solid matrix, effective thermal conductivity (k_{eff}), effective density ((ρ_{eff}) and effective specific heat ($C_{p,eff}$) have been used in the model [72].

$$\nabla \cdot \left(-k_{eff}\nabla T + (\rho C_p)_{eff} \mathbf{u}T + \sum_{i=1}^{N} h_i \mathbf{j}_i\right) = E \tag{37}$$

The first term on the left hand side refers to conduction, the second term stands for convection and the third term accounts for heat transfer due to species diffusion. The enthalpy of specie i is calculated as [73]:

$$\Delta h_i = \int_{T^{ref}}^{T} C_{p,i} \, dT \tag{38}$$

where T^{ref} is the known (reference) temperature and T is the target temperature.

Effective properties of the porous media are given by [72]:

$$(\rho C_p)_{eff} = (1 - \epsilon)\rho_s C_{p,s} + \epsilon \rho C_p \tag{39}$$

$$k_{eff} = -2k_s + \left(\frac{\epsilon}{2k_s + k} + \frac{1 - \epsilon}{3k_s}\right)^{-1} \tag{40}$$

In Eq. (37), E is the energy source term. For anode this term is given by [54,74]:

$$E_a = E_{rev_a} + E_{irr_a} + E_{ohm_e a} + E_{FOX} + E_{SR} + E_{DR} + E_{SH} \tag{41}$$

where reversible heat generation in the anode [54,75]:

$$E_{rev_a} = Tds\left(\frac{i_a}{zF}\right) \tag{42}$$

$$\frac{ds}{z} = (23.328 + 0.0042T) \tag{43}$$

irreversible heat generation in the anode [54]:

$$E_{irr_a} = \eta_{act_a} i_a \tag{44}$$

ohmic heat due to ionic resistance [54]:

$$E_{ohm_e a} = \sigma_{ea}^{eff} \nabla \phi_e \cdot \nabla \phi_e \tag{45}$$

heat produced due to full combustion of methane:

$$E_{FOX} = R_{FOX} \Delta H_{FOX} \tag{46}$$

Table 7
Reaction source terms in the electrodes.

Species	$R_{i,a}$	$R_{i,c}$
CH_4	$(-R_{FOX} - R_{SR} - R_{DR})M_{CH_4}$	$(-R_{PAR})M_{CH_4}$
H_2O	$(2R_{FOX} - R_{SR} - R_{SH})M_{H_2O} + A_a i_a(M_{H_2O}/2F)$	$(2R_{PAR})M_{H_2O}$
H_2	$(3R_{SR} + 2R_{DR} + R_{SH})M_{H_2} - A_a i_a(M_{H_2}/2F)$	0
CO	$(R_{SR} + 2R_{DR} - R_{SH})M_{CO}$	0
CO_2	$(R_{FOX} - R_{DR} + R_{SH})M_{CO_2}$	$(R_{PAR})M_{CO_2}$
O_2	$(-2R_{FOX})M_{O_2}$	$(-2R_{PAR})M_{O_2} - A_c i_c(M_{O_2}/4F)$

heat consumed due to steam reforming of methane [74]:

$$E_{SR} = R_{SR}\Delta H_{SR} \tag{47}$$

heat consumed due to dry reforming of methane:

$$E_{DR} = R_{DR}\Delta H_{DR} \tag{48}$$

heat produced due to water-gas shift reaction [74]:

$$E_{SH} = R_{SH}\Delta H_{SH} \tag{49}$$

Energy source term for the cathode is given by:

$$E_c = E_{irr_c} + E_{ohm_ec} + E_{PAR} \tag{50}$$

irreversible heat generation in the cathode [54]:

$$E_{irr_c} = \eta_{act_c} i_c \tag{51}$$

ohmic heat due to ionic resistance [54]:

$$E_{ohm_ec} = \sigma_{ec}^{eff} \nabla\phi_e \cdot \nabla\phi_e \tag{52}$$

heat produced due to parasitic combustion of methane [51]:

$$E_{PAR} = R_{PAR}\Delta H_{FOX} \tag{53}$$

2.3.3. Electrolyte

The electrolyte is impermeable to gases and allows only ionic charge transfer, so that:

$$\nabla \cdot (-\sigma_e \nabla\phi_e) = 0 \tag{54}$$

Since there is no generation of ionic or electrical current inside the electrolyte, the right hand side of the above equation is zero. Furthermore, the electrolyte is a dense, non-porous material and thus only conduction is possible. The only heat source term in the electrolyte is the ohmic resistance due to ionic current transfer [54,70].

$$\nabla \cdot (k_s \nabla T) = E \tag{55}$$

$$E_e = \sigma_e \nabla\phi_e \cdot \nabla\phi_e \tag{56}$$

2.4. Boundary conditions

The boundary conditions for each layer are given below:

2.4.1. Gas-chamber

- **Inlet**

At the inlet, an average velocity normal to the inlet boundary is prescribed:

$$\mathbf{u} = \mathbf{u_{in}} \tag{57}$$

At the inlet, the mass fraction is defined as:

$$Y_i = Y_{i_{in}} \tag{58}$$

At the inlet, the air–fuel mixture temperature is defined. Although, the mixture enters the gas-chamber at room temperature, the furnace heating in our experiments was so quick that the steady state temperature was arrived at within a few seconds. It is therefore assumed that the inlet temperature is equal to the operating furnace temperature.

$$T = T_0 \tag{59}$$

- **Axis of symmetry**

At the axis of symmetry, an axial symmetry boundary condition is applied for mass, species and energy transport. This boundary is treated as the center of the gas-chamber, i.e.:

$$r = 0 \tag{60}$$

- **Wall**

At the wall, the no-slip boundary condition is applied. A no-slip condition means that the fluid velocity is equal to the boundary velocity, which is zero in the case of a fixed wall.

$$\mathbf{u} = 0 \tag{61}$$

A mass insulation boundary condition is applied at the wall, meaning that no mass flux is allowed to cross this boundary.

$$\mathbf{n} \cdot (-\rho D_{ij}\nabla Y_i + \rho\mathbf{u}Y_i) = 0 \tag{62}$$

The wall is assumed to be at the furnace temperature.

$$T = T_0 \tag{63}$$

- **Outlet**

The outflow boundary condition is prescribed as:

$$p = p_o \tag{64}$$

The convective flux boundary condition is applied at the outlet, meaning that at the outlet boundary, the diffusion term is negligible.

$$\mathbf{n} \cdot (-\rho D_{ij}\nabla Y_i) = 0 \tag{65}$$

At the outlet, the heat transport is convection dominated. The convective heat flux boundary condition ensures that the conduction heat transfer is negligible at this boundary [54].

$$\mathbf{n} \cdot (-k\nabla T) = 0 \tag{66}$$

2.4.2. Gas diffusion electrodes

- **Anode electrode**

The current from the anode side was collected from the outlet side of the cell (i.e. 8 mm length at the end of the cell). Therefore, a zero voltage boundary condition is applied at this location.

$$\phi_s = 0 \tag{67}$$

All other outer surfaces of the anode electrode are insulated to the electrical current, hence it is assumed that there is no current flow across these boundaries.

$$\mathbf{n} \cdot (-\sigma_s^{eff}\nabla\phi_s) = 0 \tag{68}$$

- **Cathode electrode**

An operating cell voltage was applied at the cathode current collector, which was the outer layer of the cathode.

$$\phi_s = V_c \tag{69}$$

All other surfaces of the cathode electrode are insulated to the electrical current. Furthermore, ionic current cannot flow out of the electrodes. All outer surfaces of the electrodes are insulated to ionic current by applying an ionic insulation boundary condition.

$$\mathbf{n} \cdot (-\sigma_e^{eff}\nabla\phi_e) = 0 \tag{70}$$

At the outer boundaries of the cell, the radiative heat exchange boundary condition is applied between the cell and the furnace wall.

$$\mathbf{n} \cdot (\mathbf{q_1} - \mathbf{q_2}) = \epsilon_{rad}\sigma_o(T^4 - T_0^4); \quad \mathbf{q_i} = -k_i\nabla T_i + \rho_i C_{p,i}\mathbf{u_i}T_i \tag{71}$$

where ϵ_{rad} and σ_o are the radiative emissivity and Stefan–Boltzmann constant, respectively. At all interior boundaries of the cell, continuity of heat flux is maintained. This boundary condition specifies that the normal heat flux inside of the boundary is equal to the normal heat flux outside of the boundary [54].

$$(-\mathbf{n} \cdot (-k_s\nabla T))_{in} = (-\mathbf{n} \cdot (-k_s\nabla T))_{out} \tag{72}$$

Table 8
Input parameters used in the model.

Property	Symbol	Value	Units	References
Working electrical potential at anode	ϕ_{sa}	0	V	[69]
Working electrical potential at cathode	ϕ_{sc}	0.5	V	[69]
Effective anode ionic conductivity	σ_{ea}^{eff}	0.29	S m^{-1}	[69]
Effective cathode ionic conductivity	σ_{ec}^{eff}	0.24	S m^{-1}	[69]
Effective anode electronic conductivity	σ_{sa}^{eff}	4800	S m^{-1}	[69]
Effective cathode electronic conductivity	σ_{sc}^{eff}	1600	S m^{-1}	[69]
Electrolyte ionic conductivity	σ_e	$3.34 \times 10^4 exp(-10, 300/T)$	S m^{-1}	[64]
Inlet temperature	T_0	1023	K	[−]
Anodic anodic charge transfer coefficient	α_a^a	2		[69]
Anodic cathodic charge transfer coefficient	α_c^a	1		[69]
Cathodic anodic charge transfer coefficient	α_a^c	1.5		[69]
Cathodic cathodic charge transfer coefficient	α_c^c	0.5		[69]
Faraday's constant	F	96, 487	C mole^{-1}	[72]
Universal gas constant	R_g	8.314	J mole^{-1}K^{-1}	[72]
Porosity	ϵ	0.3		[54]
Tortuosity	τ	3.80		[72]
Permeability	κ	1.0×10^{-13}	m^2	[70]
Methane inlet mass fraction	$Y_{CH4_{in}}$	0.28		[−]
Oxygen inlet mass fraction	$Y_{O_{2in}}$	0.14		[−]
Operating pressure	p_o	1.013×10^5	N m^{-2}	[64]
Inlet velocity	$\mathbf{u_{in}}$	0.04	m s^{-1}	[−]
Average pore diameter	d_p	1.0	μm	[64]
Anode thermal conductivity	k_a	1.86	W m^{-1} K^{-1}	[64]
Cathode thermal conductivity	k_c	5.84	W m^{-1} K^{-1}	[64]
Electrolyte thermal conductivity	k_e	2.16	W m^{-1} K^{-1}	[64]
Anode specific heat	$C_{p,a}$	450	J kg^{-1} K^{-1}	[64]
Cathode specific heat	$C_{p,c}$	470	J kg^{-1} K^{-1}	[64]
Electrolyte specific heat	$C_{p,e}$	430	J kg^{-1} K^{-1}	[64]
Anode density	ρ_a	3310	kg m^{-3}	[64]
Cathode density	ρ_c	3030	kg m^{-3}	[64]
Electrolyte density	ρ_e	5160	kg m^{-3}	[64]
Thermal radiative diffusivity	ϵ_{rad}	0.3	−	[64]

2.4.3. Electrolyte

Since the electrolyte is impermeable to gases, both the mass flux and velocity normal to all surfaces of the electrolyte are zero.

$$\mathbf{n} \cdot \mathbf{u} = 0 \tag{73}$$

$$\mathbf{n} \cdot (-\rho D_{DG_{i,j}}^{eff} \nabla Y_i + \rho \mathbf{u} Y_i) = 0 \tag{74}$$

Continuity of ionic current is maintained at interfaces between the electrodes and electrolyte. All outer surfaces of the electrolyte are insulated to ionic current by applying an ionic insulation boundary condition.

$$\mathbf{n} \cdot (-\sigma_e \nabla \phi_e) = 0 \tag{75}$$

Continuity of heat flux is maintained at all surfaces of the electrolyte, i.e.

$$(-\mathbf{n} \cdot (-k_s \nabla T))_{in} = (-\mathbf{n} \cdot (-k_s \nabla T))_{out} \tag{76}$$

3. Numerical implementation

The model equations were solved using COMSOL Multiphysics 3.4, a commercial finite element method (FEM) based software package. The computations were performed on a 32-node Linux cluster; 32 x dual 3GHz Intel Xeon Sun Fire V60 servers each with 4 GB memory. The mesh consisted of 5746 triangular elements. The system of equations was solved simultaneously using a parametric solver (PARDISO). The cell voltage was stepped down from the open circuit voltage to the short circuit condition. The total computing time for a single I–V curve scan was approximately 35.8 min.

4. Results and discussion

The values of various electrochemical/hydrodynamic transport parameters along with the fitting parameters are given in

Table 9
Fitting parameters.

Property	Symbol	Value	Units
Anodic pre-exponential coefficient	γ_a	$1.4e^{-7}$	−
Cathodic pre-exponential coefficient	γ_c	$2.7e^{-7}$	−
Anodic activation energy	$E_{act,a}$	130	J mol^{-1}
Cathodic activation energy	$E_{act,c}$	190	J mol^{-1}
Anode active surface area	A_a	$1.05e^7$	m^{-1}
Cathode active surface area	A_c	$4.25e^6$	m^{-1}
Methane parasitic index	d	0.1	−
Oxygen parasitic index	f	0.2	−

Tables 8 and 9. The governing equations and the corresponding source terms are summarized in Tables 10 and 11. The results presented in all figures are based on parameters listed in Tables 8 and 9, unless stated otherwise.

The experimental data obtained in our earlier study (Ref. [42]) were used to calibrate the model. The cell was operated with a

Table 10
Computational domain and governing equations.

Domain	Equations solved
Ω_{GC}	$\nabla \cdot (\rho \mathbf{u}) = 0$ $\rho(\mathbf{u} \cdot \nabla)\mathbf{u} = -\nabla p + \mu \nabla^2 \mathbf{u} + \frac{1}{3}\mu \nabla(\nabla \cdot \mathbf{u})$ $\nabla \cdot (\rho \mathbf{u} Y_i + \mathbf{j}_i) = 0$ $\nabla \cdot (-k\nabla T + \rho C_p \mathbf{u} T + \sum_{i=1}^{N} h_i \mathbf{j}_i) = 0$
$\Omega_{a,c}$	$\nabla \cdot (\rho \mathbf{u}) = 0$ $\frac{\mu}{\kappa}\mathbf{u} = -\nabla p + \mu \nabla^2 \mathbf{u} + \frac{1}{3}\mu \nabla(\nabla \cdot \mathbf{u}) + \mathbf{F}$ $\nabla \cdot (\rho \mathbf{u} Y_i + \mathbf{j}_i) = R_i$ $\nabla \cdot (-\sigma_s^{eff} \nabla \phi_s) = Q_s$ $\nabla \cdot (-\sigma_e^{eff} \nabla \phi_e) = Q_e$ $\nabla \cdot (-k_{eff} \nabla T + (\rho C_p)_{eff} \mathbf{u} T + \sum_{i=1}^{N} h_i \mathbf{j}_i) = E$
Ω_e	$\nabla \cdot (-\sigma_e \nabla \phi_e) = 0$ $\nabla \cdot (-k_s \nabla T) = E$

Table 11
Source terms defined in Table 10.

Source term	Anode	Electrolyte	Cathode
F	$R_{i,a}\mathbf{u}$	–	$R_{i,c}\mathbf{u}$
Q_s	$-A_a i_a$	–	$+A_c i_c$
Q_e	$-A_a i_a$	0	$+A_c i_c$
E	$E_{rev,a} + E_{irr,a} + E_{ohm,a} + E_{FOX} + E_{SR} + E_{DR} + E_{SH}$	$E_{ohm,e}$	$E_{irr,c} + E_{ohm,c} + E_{PAR}$

methane/air mixture of 25/60 mL min^{-1} at a temperature of 750 °C. With the help of various fitting parameters as given in Table 9, a good match was obtained between the experimental and model predicted performance curves (Fig. 2). A slight discrepancy between the experiment and the model was observed at higher current densities perhaps due to carbon (electrochemical) gasification that generates additional current. Since this model does not consider carbon formation, this mismatch at higher current densities is attributed to this effect.

In Fig. 3(a), the velocity field in the gas chamber is shown. It can be seen that the velocity around the cell and inside the micro-tube significantly differs than at the gas-chamber inlet. In Fig. 3(b), the velocity profile inside the micro-tube and both electrodes (anode and cathode) has been shown along the axial direction. From this plot, it is evident that the gas velocity inside the micro-tube is significantly reduced and approaching to zero. The gas velocity in both electrodes is almost zero, showing that the mass transport inside the electrodes is mainly diffusive. The reduced velocity in the electrodes is due to the porous nature of the electrodes providing limited passage for the gas flow. This low gas velocity resulted in mass transport limitation on the anode side due to insufficient gas supply to the anode electrode. Furthermore, anode chemistry is much more complicated than the cathode, so that severe fuel depletion is likely to happen in such a small volume. Our experimental results (Ref. [42]) show that micro-tubular geometry can compete other designs such as planar, co-planar in terms of effective fuel utilization. The current modelling study clearly shows that the design opted in our experimental study was not optimized and there is a possibility of further improvement in the fuel utilization. The mass transport limitation due to very low gas velocity inside the micro-tube is the main culprit in lowering the performance. Due to this limitation, it is not appropriate to compare the performance of micro-tube under single-chamber conditions with that under dual-chamber (conventional) operation. In order to improve the performance under single-chamber conditions, parametric study related to the geometry and cell positioning is important, which will be discussed later.
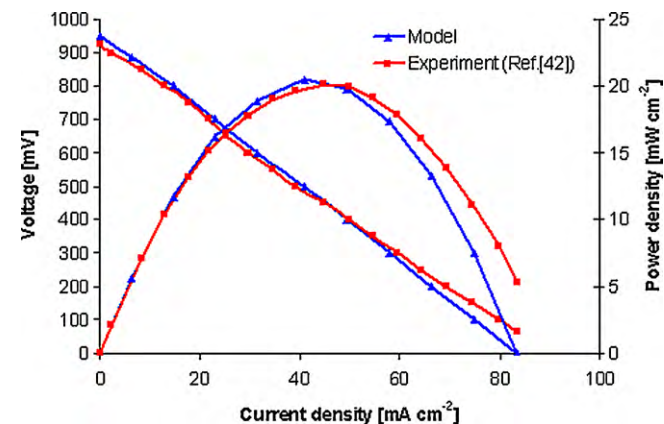
In Fig. 4, the mass fraction of different species is plotted at methane-to-oxygen ratio, R_{mix} = 2.0 and operating voltage of 0.5 V in the anode along the axial direction. As can be seen, the mass fraction of each species remains unchanged until it reaches the cell. The methane is nearly consumed in the anode via full combustion reaction producing water vapor and carbon dioxide. The increase in carbon dioxide mass fraction near the cell inlet clearly shows that the methane combustion precedes at that location. The decrease in carbon dioxide mass fraction downstream indicates that methane dry reforming is dominating. The water produced via methane full combustion and electrochemistry is balanced by its consumption via steam reforming and water-gas shift reaction. The production of hydrogen via reforming and water-gas shift reactions is balanced by its electrochemical consumption, whereas the net carbon monoxide production is a result of its production via reforming reactions and consumption via water-gas shift reaction. The decrease in oxygen mass fraction on the anode side is due to methane combustion consuming oxygen.

Fig. 5 shows the mass fraction of oxygen in the cathode at different R_{mix} values along the gas-chamber length. As can be seen, slight dips and peaks are observed at the cell edges, where the gaseous mixtures splits-up. Some is directed towards the anode,
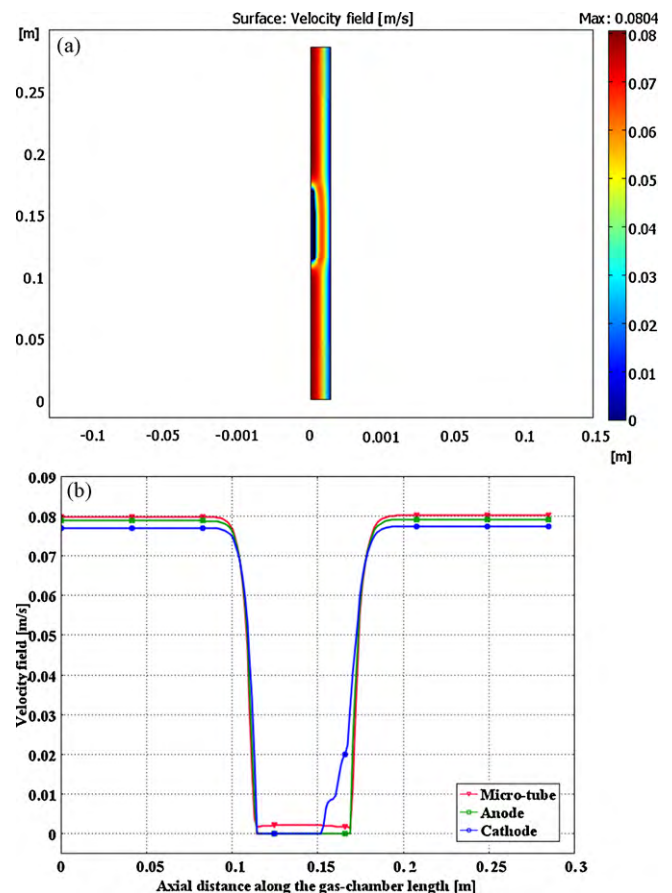

Fig. 2. Simulated vs. experimental performance curve for R_{mix} = 2.0 and at an operating temperature of 750 °C.

Fig. 3. (a) Velocity profile in the gas-chamber. (b) Velocity field inside micro-tube and electrodes along the gas-chamber length.
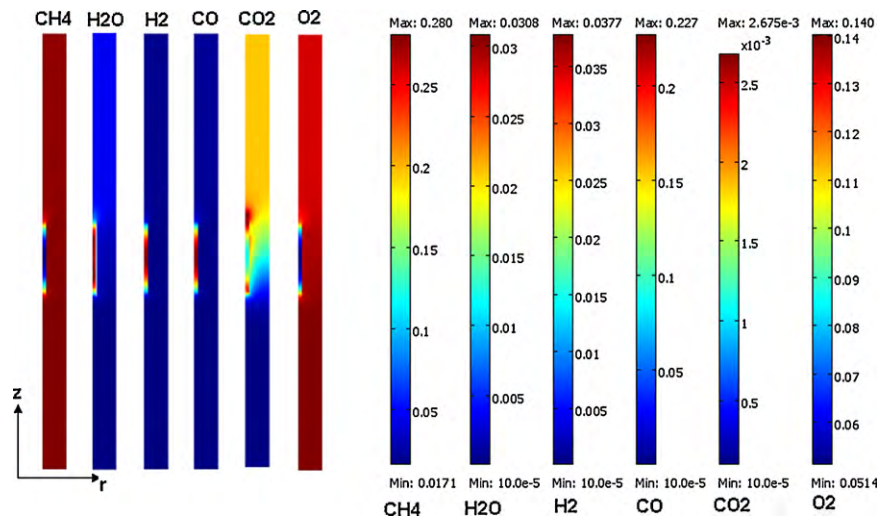
Fig. 4. Mass fraction of different species in the gas-chamber at $R_{mix} = 2.0$ and 0.5 V.

the remainder passing over the cathode and then recombining. Due to parasitic combustion and electrochemical oxygen consumption, there is a reduction in oxygen mass fraction along the cell length. Furthermore, the oxygen consumption increases with decrease in R_{mix} value. This behavior is often observed in experiments as the decrease in mixing ratio supplies additional oxygen which promotes full combustion. Ideally, there should be no oxygen on the anode side and maximum oxygen on the cathode side in order to generate maximum oxygen partial pressure differential across the electrodes. However, in practice the electrodes are non-selective and parasitic combustion occurs which lowers the cell performance. From the above argument, it is clear that the cathode's selectivity and anode's catalytic activity are important factors in improving the cell performance.

Fig. 6 shows the electronic current density along the anode–electrolyte interface at various operating voltages. As can be seen, the current density is highly non-uniform over the cell length. This highly non-uniform local current density distribution affects the average value of the current density as shown in the performance curves. In order to reduce this non-uniformity, the current collection from the anode side must be made throughout the anode length. As shown in Fig. 6, the current density is minimum at the cell edges, increases from the cell inlet, reaches to its maximum near the cathode outlet and remains constant for up to 10 mm before

dropping to zero at the electrolyte outer edge. Furthermore, there is a steep increase in the current density at lower operating voltages due to lower resistance at these voltages. It is also clear that the current prefers the shortest conduction path. Therefore current density is higher in the vicinity of the current collection point at the electrolyte outer edge.

In Fig. 7, the ionic current density distribution in the electrolyte is shown at various operating voltages. As can be seen, the ionic current density is uniform over the cell length. The ionic current density increases with decrease in operating voltage, dropping to zero near the cathode outer edge. The very low values of ionic current densities as compared to the electronic current densities are due to low ionic conductivity of the electrolyte in comparison with the electronic conductivity of the electrodes.

Fig. 8 shows the performance curves calculated from the geometrical parametric study. The results shown in this figure show the effect of change in micro-tube diameter (D_t), gas-chamber length (L_c) and the gas-chamber diameter (D_c). The computed performance curves are compared with the standard (base-case) geometry i.e. having dimensions D_t, L_c and D_c as given in Table 3. The results show that reducing the diameter of the micro-tube is effective in improving the maximum power density (MPD). By reducing the micro-tube diameter to one-half, the MPD was increased by 4.60%(For interpretation of the references to colour in this text, the reader is referred to the web version of the arti-
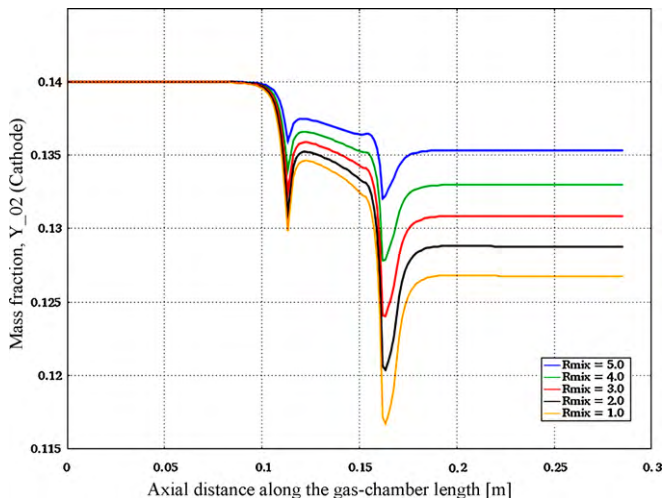

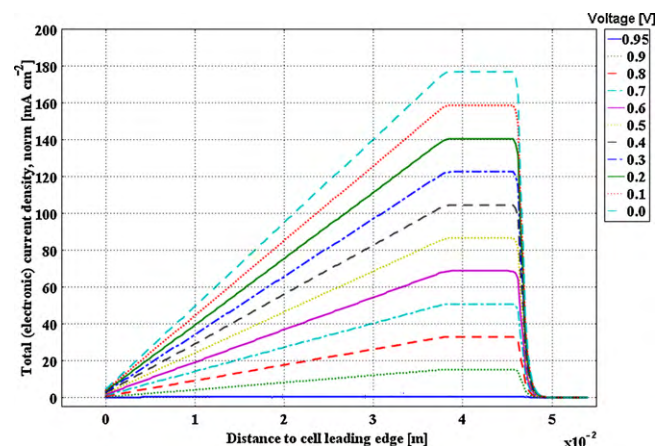**Fig. 5.** Mass fraction plot of oxygen in the cathode at different mixing ratios at 0.5 V.

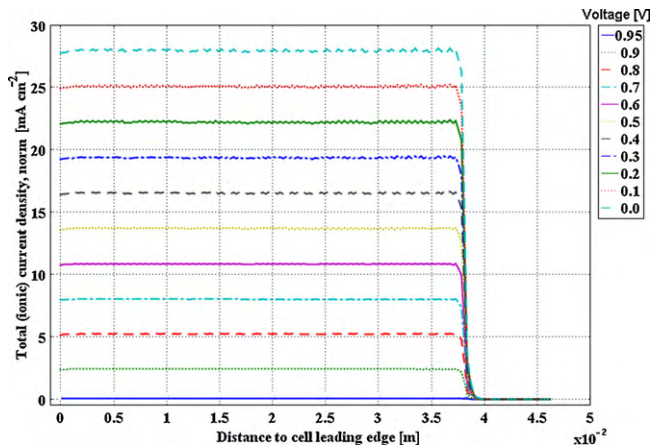**Fig. 6.** Distribution of electronic current density at the anode–electrolyte interface at different operating voltages.

Fig. 7. Distribution of ionic current density within the electrolyte at different operating voltages.
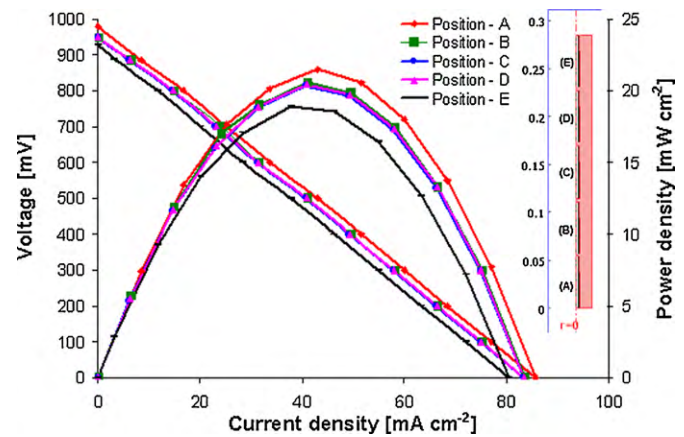

Fig. 9. Effect of cell positioning on the performance curves.

cle.)(red curve). Doubling the cell diameter decreased the MPD by 3.95% (pink curve). Although, it looks like that decrease in micro-tube diameter increases the flow resistance, thereby reducing the flow velocity inside the micro-tube. However, this argument is only valid for laminar, steady, incompressible and isothermal flow inside a single tube or pipe. In the current study, the situation is rather different; the flow is in between two concentric pipes (gas-chamber and micro-tube) and there is a change of diameter as soon the flow approaches the micro-tube. The effect of change in diameter (of the micro-tube) is best correlated with the effect of a flow passing through a nozzle. The continuity of flow applies here and reduction in diameter gives increase in velocity. The other reason could be that the flowing medium is gas (compressible) and due to sudden temperature increase at the inlet because of combustion, there will be expansion phenomenon occurring which will accelerate the flow. The model is thermo-fluid coupled, this effect would be another contributor for increase in velocity inside the micro-tube. The increased velocity inside the micro-tube (by keeping the gas-chamber inlet velocity unchanged) enhances the mass transport and lowers the diffusion losses on the anode side which results in improved MPD. Contrary to this, halving the gas-chamber diameter decreases the MPD by 1.90% (yellow curve). In addition, the model predicts that the change in the length of the gas-chamber has minimal effect on the MPD value.

In Fig. 9, the performance curves are shown as a function of the cell position. Five positions, namely A–E were simulated. The positions A and E refer to cell location at the inlet and outlet of the

gas-chamber, respectively. The position C is the standard (base-case) position with cell located in the middle of the gas-chamber. The positions B and D are in the middle of A–C and C–E positions, respectively. As can be seen, when the cell is placed in position A at the inlet of the gas-chamber, the MPD improves by 5.17%(For interpretation of the references to colour in this text, the reader is referred to the web version of the article.)(red curve). By contrast, when the cell is located at the outlet (position E), the MPD drops by 7.33% (black curve). On the other hand, positions B–D have minimal effect in changing the MPD value. The improvement in cell performance at position A is due to increase in velocity at the cell inlet as compared to the other positions. The comparatively poor performance in position E is due to low gas velocity and greater bypass at that location. Furthermore, in real experiments, the back pressure may affect the cell performance significantly due to ambient air back diffusion. The gas-chamber wall friction may also reduce the gas velocity during experiments. Therefore, this position is not preferred.

In Fig. 10, the temperature profile (on the anode surface) along the cell length is shown. As can be seen, the calculated temperature decreases up to the complete cathode length (39 mm), and then increases along the remaining cell length. In our experimental study (Ref. [42]), we measured the temperature profiles up to the cathode active length and the measurements fitted the calculated temperature profile. This result shows that the reaction chemistry chosen on the anode side is appropriate and the model results are reliable. The increase in calculated temperature for the remaining cell length is due to the presence of anode current collection which generates additional resistive heat.
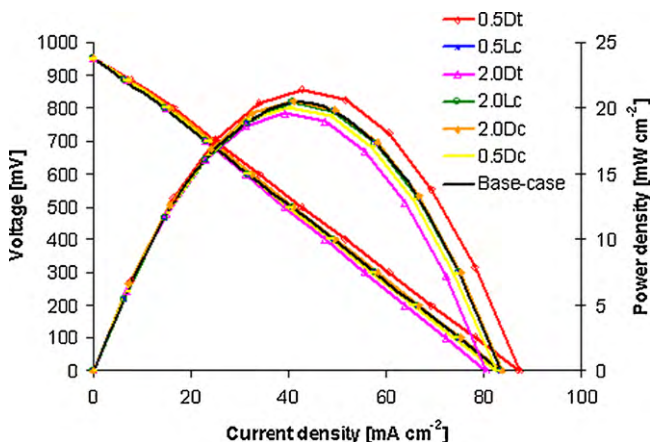

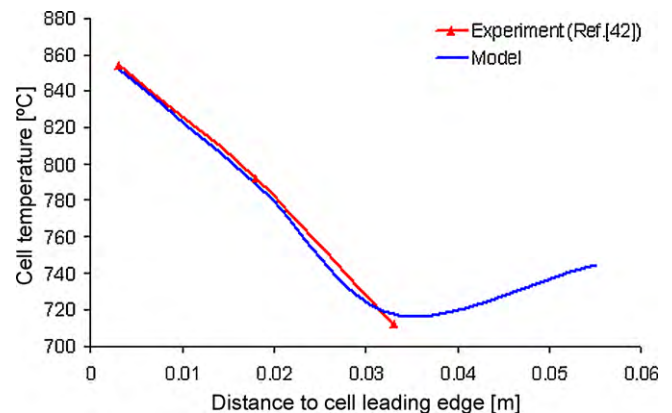**Fig. 8.** Effect of geometrical parameters on the performance curves.

Fig. 10. Calculated vs. measured temperature profile at cell temperature of 750 °C.

5. Conclusions

A two-dimensional, axisymmetric, numerical model of a micro-tubular, single-chamber solid oxide fuel cell (MT-SC-SOFC) has been developed. The model considers, methane full combustion followed by steam and dry reforming of methane with water-gas shift reaction producing additional hydrogen. The cathode side considers methane parasitic combustion along with the electrochemical reduction of oxygen. The results show that the poor performance of MT-SC-SOFC as compared to the conventional (dual-chamber) MT-SOFC is connected to the mass transport limitation on the anode side. The gas velocity inside the micro-tube is far lower than that at the gas-chamber inlet. Furthermore, the current density along the cell length is highly non-uniform, suggesting that the anode current collection should be made throughout the anode length or the cell length must be shortened in order to make the current density as uniform as possible.

The calculated and measured temperature profiles are in good agreement, indicating the appropriate selection of anode side chemistry. With the help of calculated performance curves, the model was validated against our earlier experimental study. The results show that the model is able to predict the experimental trends and is reliable for optimization of the experimental setup.

Acknowledgments

References

[1] H. Yokokawa, H. Tu, B. Iwanschitz, A. Mai, J. Power Sources 182 (2008) 400–412.
[2] V. Karakoussis, N.P. Brandon, M. Leach, R. van der Vorst, J. Power Sources 101 (2001) 10–26.
[3] M. Ni, D.Y.C. Leung, M.K.H. Leung, Int. J. Hydrogen Energy 33 (2008) 5765–5772.
[4] C. Lu, S. An, W.L. Worrell, J.M. Vohs, R.J. Gorte, Solid State Ionics 175 (2004) 47–50.
[5] W. Zhou, R. Ran, Z. Shao, J. Power Sources 192 (2009) 231–246.
[6] F. Nishiwaki, T. Inagaki, J. Kano, J. Akikusa, N. Murakami, K. Hosoi, J. Power Sources 157 (2006) 809–815.
[7] T. Inagaki, F. Nishiwaki, S. Yamasaki, T. Akbay, K. Hosoi, J. Power Sources 181 (2008) 274–280.
[8] X.W. Zhang, S.H. Chan, G. Li, H.K. Ho, J. Li, Z. Feng, J. Power Sources 195 (2010) 685–702.
[9] T. Horita, Y. Xiong, H. Kishimoto, K. Yamaji, N. Sakai, H. Yokokawa, J. Power Sources 131 (2004) 293–298.
[10] K. Eguchi, H. Kojo, T. Takeguchi, R. Kikuchi, K. Sasaki, Solid State Ionics 152–153 (2002) 411–416.
[11] P. Aguiar, C.S. Adjiman, N.P. Brandon, J. Power Sources 138 (2004) 120–136.
[12] F. Tietz, H.-P. Buchkremer, D. Stover, Solid State Ionics 152–153 (2002) 373–381.
[13] H. Itoh, M. Mori, N. Mori, T. Abe, J. Power Sources 49 (1994) 315–332.
[14] M. Ippommatsu, H. Sasaki, S. Otoshi, Int. J. Hydrogen Energy 21 (1996) 129–135.
[15] Y. Hao, D.G. Goodwin, J. Power Sources 183 (2008) 157–163.
[16] T. Suzuki, T. Yamaguchi, Y. Fujishiro, M. Awano, J. Power Sources 163 (2007) 737–742.
[17] T. Suzuki, Y. Funahashi, Z. Hasan, T. Yamaguchi, Y. Fujishiro, M. Awano, Electrochem. Commun. 10 (2008) 1563–1566.
[18] N. Akhtar, S.P. Decent, D. Loghin, K. Kendall, J. Power Sources 193 (2009) 39–48.
[19] M. Liu, Z. Lu, B. Wei, R. Zhu, X. Huang, K. Chen, G. Ai, W. Su, J. Electrochem. Soc. 154 (2007) B588–B592.
[20] T. Suzuki, P. Jasinski, V. Petrovsky, H.U. Anderson, F. Dogan, J. Electrochem. Soc. 151 (2004) A1473–A1476.
[21] T. Hibino, A. Hashimoto, M. Yano, M. Suzuki, S. Yoshida, M. Sano, Electrochem. Soc. 149 (2002) A133–A136.
[22] P. Jasinski, T. Suzuki, F. Dogan, H.U. Anderson, Solid State Ionics 175 (2004) 35–38.
[23] T. Hibino, H. Tsunekawa, S. Tanimoto, M. Sano, J. Electrochem. Soc. 147 (2000) 1338–1343.
[24] K. Asano, T. Hibino, H. Iwahara, J. Electrochem. Soc. 142 (1995) 3241–3245.
[25] T. Hibino, A. Hashimoto, M. Suzuki, M. Yano, S. Yoshida, M. Sano, J. Electrochem. Soc. 149 (2002) A195–A200.
[26] T.W. Napporn, X.J. Bedard, F. Morin, M. Meunier, J. Electrochem. Soc. 151 (2004) A2088–A2094.
[27] X.J. Bedard, T.W. Napporn, R. Roberge, M. Meunier, J. Power Sources 153 (2006) 108–113.
[28] T. Suzuki, P. Jasinski, V. Petrovsky, H.U. Anderson, F. Dogan, J. Electrochem. Soc. 152 (2005) A527–A531.
[29] M. Yano, A. Tomita, M. Sano, T. Hibino, Solid State Ionics 177 (2007) 3351–3359.
[30] T. Suzuki, P. Jasinski, H.U. Anderson, F. Dogan, J. Electrochem. Soc. 151 (2004) A1678–A1682.
[31] I.C. Stefan, C.P. Jacobson, S.J. Visco, L.C. De Jonghe, Electrochem. Solid-State Lett. 7 (2004) A198–A200.
[32] A. Tomita, D. Hirabayashi, T. Hibino, M. Nagao, M. Sano, Electrochem. Solid-State Lett. 8 (2005) A63–A65.
[33] S. Asahara, D. Michiba, M. Hibino, T. Yao, Electrochem. Solid-State Lett. 8 (2005) A449–A451.
[34] B.E. Buergler, M.E. Siegrist, L.J. Gauckler, Solid State Ionics 176 (2005) 1717–1722.
[35] M. Yano, T. Kawai, K. Okamoto, M. Nagao, M. Sano, A. Tomita, T. Hibino, J. Electrochem. Soc. 154 (2007) B865–B870.
[36] M. Yano, M. Nagao, K. Okamoto, A. Tomita, Y. Uchiyama, N. Uchiyama, T. Hibino, Electrochem. Solid-State Lett. 11 (2008) B29–B33.
[37] M. Ni, D.Y.C. Leung, M.K.H. Leung, J. Power Sources 183 (2008) 133–142.
[38] T. Hibino, S. Wang, S. Kakimoto, M. Sano, Electrochem. Solid-State Lett. 2 (1999) 317–319.
[39] T. Hibino, A. Hashimoto, T. Inoue, J. Tokuno, S. Yoshida, M. Sano, J. Electrochem. Soc. 147 (2000) 2888–2892.
[40] B.E. Buergler, A.N. Grundy, L.J. Gauckler, J. Electrochem. Soc. 153 (2006) A1378–A1385.
[41] Y. Hao, D.G. Goodwin, J. Electrochem. Soc. 155 (2008) B666–B674.
[42] N. Akhtar, S.P. Decent, K. Kendall, J. Power Sources 195 (2010) 7818–7824.
[43] B. Li, K. Maruyama, M. Nurunnabi, K. Kunimori, K. Tomishige, Ind. Eng. Chem. Res. 44 (2005) 485–494.
[44] B. Li, R. Watanabe, K. Maruyama, M. Nurunnabi, K. Kunimori, K. Tomishige, Appl. Catal. A 290 (2005) 36–45.
[45] K. Tomishige, S. Kanazawa, K. Suzuki, M. Asadullah, M. Sato, K. Ikushima, K. Kunimori, Appl. Catal. A 233 (2002) 35–44.
[46] B. Li, R. Watanabe, K. Maruyama, K. Kunimori, K. Tomishige, Catal. Today 104 (2005) 7–17.
[47] K. Tomishige, M. Nurunnabi, K. Maruyama, K. Kunimori, Fuel Process. Technol. 85 (2004) 1103–1120.
[48] K. Tomishige, S. Kanazawa, K. Suzuki, M. Asadullah, M. Sato, K. Ikushima, K. Kunimori, Appl. Catal. A 351 (2008) 54–58.
[49] K. Yoshida, K. Okumura, T. Miyao, S. Naito, S. Ito, K. Kunimori, K. Tomishige, Appl. Catal. A 351 (2008) 217–225.
[50] Z. Shao, J. Mederos, W.C. Chueh, S.M. Haile, J. Power Sources 162 (2006) 589–596.
[51] Y. Hao, Z. Shao, J. Mederos, W. Lai, D.G. Goodwin, S.M. Haile, Solid State Ionics 177 (2006) 2013–2021.
[52] B. Todd, J.B. Young, J. Power Sources 110 (2002) 186–200.
[53] I. Riess, J. Power Sources 175 (2008) 325–337.
[54] L. Andreassi, G. Rubeo, S. Ubertini, P. Lunghi, R. Bove, Int. J. Hydrogen Energy 32 (2007) 4559–4574.
[55] W.G. Bessler, S. Gewies, J. Electrochem. Soc. 154 (2007) B548–B559.
[56] T. Berning, D.M. Lu, N. Djilali, J. Power Sources 106 (2002) 284–294.
[57] B.R. Sivertsen, N. Djilali, J. Power Sources 141 (2005) 65–78.
[58] R. Taylor, R. Krishna, Multicomponent Mass Transfer, John Wiley and Sons, 1993.
[59] R. Perry, D. Green, Perry's Chemical Engineering Handbook, sixth ed., McGraw-Hill, 1983.
[60] L.E. Sissom, D.R. Pitts, Elements of Transport Phenomena, international student ed., McGraw-Hill, 1972.
[61] J.M. Coulson, J.F. Richardson, Fluid flow, heat transfer and mass transfer, fifth ed., vol. 1, Butterworth-Heinemann, Oxford, 1996.
[62] D.F. Cheddie, N.D.H. Munroe, J. Power Sources 160 (2006) 215–223.
[63] M.F. Serincan, U. Pasaogullari, N.M. Sammes, J. Electrochem. Soc. 155 (2008) B1117–B1127.
[64] D.D. Cui, Y.C. Chung, L. Liu, Y. Dong, M. Cheng, J. Power Sources 174 (2007) 246–254.
[65] M.E.E. Abashar, Int. J. Hydrogen Energy 29 (2004) 799–808.
[66] M. Ghadrdan, H. Mehdizadeh, Proc. COMSOL Conference, Hannover, Germany, 2008.
[67] X.E. Verykios, Int. J. Hydrogen Energy 28 (2003) 1045–1063.
[68] P. Ivanov, Electrochim. Acta 52 (2007) 3921–3928.
[69] J.I. Gazzarri, O. Kesler, J. Power Sources 167 (2007) 430–441.
[70] G.H. Guvelioglu, H.G. Stenger, J. Power Sources 147 (2005) 95–106.
[71] S. Liu, C. Song, Z. Lin, J. Power Sources 183 (2008) 214–225.
[72] V.M. Janardhanan, O. Deutschmann, Chem. Eng. Sci. 6 (2007) 5473–5486.
[73] I. Zinovik, D. Poulikakos, Electrochim. Acta 54 (2009) 6234–6243.
[74] J. Li, G.-Y. Cao, X.-J. Zhu, H.-Y. Tu, J. Power Sources 171 (2007) 585–600.
[75] D.F. Cheddie, N.D.H. Munroe, J. Power Sources 171 (2007) 634–643.